

Validation of Coronal Mass Ejection Arrival-time Forecasts by Magnetohydrodynamic Simulations Based on Interplanetary Scintillation Observations

Kazumasa Iwai (✉ k.iwai@isee.nagoya-u.ac.jp)

Nagoya University <https://orcid.org/0000-0002-2464-5212>

Daikou Shiota

joho tsushin kenkyu kiko

Munetoshi Tokumaru

Nagoya Daigaku

Ken'ichi Fujiki

Nagoya Daigaku

Mitsue Den

joho tsushin kenkyu kiko

Yûki Kubo

Joho Tsushin Kenkyu Kiko

Express Letter

Keywords: interplanetary scintillation, coronal mass ejection, space weather forecasting, magnetohydrodynamics, data assimilation

Posted Date: June 2nd, 2020

DOI: <https://doi.org/10.21203/rs.3.rs-32257/v1>

License: © ⓘ This work is licensed under a Creative Commons Attribution 4.0 International License. [Read Full License](#)

Version of Record: A version of this preprint was published on January 6th, 2021. See the published version at <https://doi.org/10.1186/s40623-020-01345-5>.

Abstract

Coronal mass ejections (CMEs) cause various disturbances of the space environment; therefore, forecasting their arrival time is very important. However, forecasting accuracy is hindered by limited CME observations in interplanetary space. This study investigates the accuracy of CME arrival times at the Earth forecasted by three-dimensional (3D) magnetohydrodynamic (MHD) simulations based on interplanetary scintillation (IPS) observations. In this system, CMEs are approximated as spheromaks with various initial speeds. Ten MHD simulations with different CME initial speed are tested, and the density distributions derived from each simulation run are compared with IPS data observed by the Institute for Space-Earth Environmental Research (ISEE), Nagoya University. The CME arrival time of the simulation run that most closely agrees with the IPS data is selected as the forecasted time. We then validate the accuracy of this forecast using 12 halo CME events. The average absolute arrival-time error of the IPS-based MHD forecast is approximately 5.0 h, which is one of the most accurate predictions that ever been validated, whereas that of MHD simulations without IPS data, in which the initial CME speed is derived from white-light coronagraph images, is approximately 6.7 h. This suggests that the assimilation of IPS data into MHD simulations can improve the accuracy of CME arrival-time forecasts. The average predicted arrival times are earlier than the actual arrival times. These early predictions may be due to overestimation of the magnetic field included in the spheromak and/or underestimation of the drag force from the background solar wind, the latter of which could be related to underestimation of CME size or background solar wind density.

Introduction

Coronal mass ejections (CMEs) are eruptions of magnetized plasma structures generated by solar eruptive phenomena such as flares. CMEs occasionally reach Earth and cause various disturbances of the space environment, where a vast amount of social infrastructure is in operation. Therefore, forecasting the arrival time of CMEs is an important topic in the field of space weather research.

Many studies have attempted to forecast CME arrival using empirical models (e.g. Gopalswamy et al. 2001), and global magnetohydrodynamic (MHD) simulations of the heliosphere such as ENLIL (Odstrcil 2003), SUSANOO (Shiota et al. 2014; Shiota and Kataoka 2016), and EUFORIA (Pomoell and Poedts 2018). These simulations calculate the background solar wind from magnetic field data of the solar surface and empirical models of the solar wind speed (Wang and Sheeley 1990, Arge and Pizzo 2000, Arge et al. 2004). Then, the simulations approximate the CMEs as simple structures such as cones or spheromaks. The modeled CMEs are placed at the inner boundary, which is approximately a few tens of solar radii (R_s), and their propagation is simulated to 1 AU.

The accuracy of CME arrival-time forecasts has been statistically validated in previous studies (e.g., Wold et al. 2018), which suggest an error of more than 10 h for current MHD simulations. There are many possible causes of this arrival-time error. Ambiguity of the modeled CME parameters is the first candidate. Many studies use white-light coronagraph images, which are typically provided by the Large Angle and Spectrometric Coronagraph (LASCO: Brueckner et al. 1995) onboard the Solar and Heliospheric Observatory (SOHO), to detect CMEs and derive characteristics such as CME speed, width, and tilt angle for input into CME models (Wold et al. 2018 and references therein). However, these observations typically contain errors due to the projection effect (Temmer et al. 2009). In fact, some studies have suggested that forecasting accuracy can be improved by deriving the input parameters from multiple spacecraft observations (Millward et al. 2013) or by using the heliospheric imager (HI) onboard Solar Terrestrial Relations Observatory (STEREO) satellites (Mostl et al. 2014). There are many other potential reasons for the observed arrival-time error, such as interaction between CMEs and background solar wind, accuracy of the simulated background solar wind, and CME-CME interactions during propagation (e.g., Möstl et al. 2014; Millward et al. 2013.; Lee et al. 2013).

Turbulence contained in the solar wind plasma can scatter radio emission from extra-galactic radio sources, which is known as interplanetary scintillation (IPS, Hewish et al. 1964). Rapidly propagating CMEs sweep the background solar wind, forming dense regions in front of the CMEs. These regions can significantly scatter radio emissions. Hence, IPS observations can be used to detect CMEs propagating in interplanetary space (e.g., Tokumaru et al. 2003; 2005; Manoharan 2006; Glyantsev et al. 2015; Johri and Manoharan 2016). IPS data are also used as additional information for the inner boundary of global MHD simulations (Jackson et al. 2015; Yu et al. 2015).

Iwai et al. (2019) developed a new CME forecasting system that combines MHD simulations (SUSANOO-CME; Shiota and Kataoka 2016) with IPS observations at 327 MHz. They used this system to investigate a CME generated by an X9.3 flare on September 6, 2017. After comparing IPS data with that estimated by multiple CME simulations under different initial conditions, they found that the CME simulation that best estimates the IPS observation can more accurately predict the CME arrival time on Earth.

The accuracy of arrival-time forecasts using real-time MHD simulations can be improved by incorporating IPS data because the IPS can observe CMEs in the interplanetary space, whereas their statistical accuracy under the real-time operation should be evaluated to include the IPS based simulation to the space weather forecasting system. Therefore, the purpose of this study is to evaluate the performance of the SUSANOO-CME model combined with IPS data for real-time forecasting. To do this, we simulate the arrival times of CMEs using MHD simulations with and without IPS data, and compare their accuracy.

Methods

MHD simulation (SUSANOO-CME)

In this study, we used a 3D global MHD simulation of the inner heliosphere called SUSANOO-CME. Details of this simulation system have been described in previous studies (Shiota et al. 2014; Shiota and Kataoka 2016; Iwai et al. 2019); therefore, we only summarize the basics of the system here. The simulation region is a spherical shaped inner heliosphere between 25 and 425 R_s , formed by a Yin-Yang grid (Kageyama and Sato 2004). At the inner boundary, the magnetic field, velocity, density, and temperature of the background solar wind are given by the potential field source surface (PFSS) approximation from the models of the solar wind (Arge and Pizzo 2000; Hayashi et al. 2003).

A CME was approximated as a spheromak and placed on the inner boundary. The initial parameters of the spheromak were defined from the Geostationary Operational Environmental Satellite (GOES) and LASCO observational data to enable automatic operation in real-time. The location and onset time of the CME were approximated to those of the corresponding X-ray flare observed by GOES. We assumed that the magnetic flux included in the spheromak was proportional to the corresponding X-ray flux and set 3.0 , 1.0 , and $0.3 \times 10^{21} Mx$ for X, M, and C class flares, respectively. The radial and angular widths of the spheromak were also defined from the X-ray flux as follows: radial width = 2, 3, and 4 R_s and angular width = 30, 60, and 90° for CMEs with X, M, and C class flares, respectively. The tilt angle of the spheromak was 90° for all CMEs.

In this study, we focus on the initial speed of the CMEs, which was employed as the only free parameter in the MHD simulations. For each CME event, we employed 10 simulations with different CME initial speed; the maximum speed derived from the Computer Aided CME Tracking software (CACTus: Robbrecht and Berghmans 2004), the initial speed listed in the LASCO catalog (Yashiro et al. 2004), and 8 other simulations with initial speeds that were faster or slower than the CME speed in the LASCO CME catalog in 100-km/s intervals.

The simulation period started two days before and ended four days after the CME onset. The simulation also contained CMEs observed within two days of the CME of interest in order to determine the effect of CME-CME interactions. The initial speeds of these CMEs were fixed to those listed in the LASCO CME catalog so they have no free parameters.

IPS observations

IPS observations were conducted by the Institute for Space-Earth Environmental Research (ISEE), Nagoya University. We used the g-value of IPS (Gapper et al. 1982) obtained from the Solar Wind Imaging Facility (SWIFT: Tokumaru et al 2011), which is one of the three large IPS radio telescopes of ISEE. This telescope observes 50–70 radio sources each day throughout the year at an observation frequency of 327 MHz, which is able to detect the IPS signatures of solar wind between 0.2 AU and 1.0 AU.

IPS estimation using MHD simulations

The IPS g-value was estimated from the 3D density distribution obtained from the SUSANOO-CME simulation, as described in Iwai et al. (2019). In this system, the radio scintillation of each radio source is calculated from the density distribution along the line of sight to the radio source assuming a weak scattering condition (Young 1971). We also assumed that the density fluctuation included in the solar wind was proportional to the density of the solar wind. Figure 1 shows an example of the estimated IPS g-value distribution on the sky plane. The high g-value region, which indicates a high-density region along the line of sight, has a loop-like distribution. This is because the fast propagating spheromak sweeps the background solar wind, forming a high-density region at the front of the spheromak (Iwai et al. 2019).

Once we set the range of initial parameters of the spheromak (e.g., speed, location, widths), we are able to restrict the possible location range of the spheromak at any given time. Therefore, we selected ranges for the time period, elongation, and position angle of the radio source, as indicated by the white circles and red lines in Fig. 1. We selected the radio sources included in the partial torus surrounded by the red lines, and compared the observed and simulated g-value for a given time.

The IPS g-value describes the ratio between the typical IPS amplitude around the observation period and the IPS amplitude observed at a given moment. Therefore, if the front of the CME passes the line of sight to the radio source, the observed g-value should be larger than 1. We selected a radio source with $g > 1$ included in the partial torus, which may be able to detect the CME. Then, we derived the positional difference between the radio source and the g-value peak of the simulation along the same position angle. Then, we derived the average positional difference of all selected radio sources for each simulation run. The simulation run that estimated the IPS g-value most consistently, i.e., the simulation run with the smallest average positional difference, was deemed the most reliable simulation, and was selected as the solution of the IPS-based SUSANOO-CME simulation. The CME arrival time of each simulation is detected using the onset of the velocity enhancement at the position of the Earth as shown in Fig. 2. Finally, the accuracy of the CME arrival time of each simulation was evaluated by comparing the spheromak arrival time at the Earth with the observed shock arrival time at the Earth using the OMNI data.

Data set

We selected CMEs for arrival-time validation according to the following selection criteria. The CMEs were halo CMEs observed between January 2013 and December 2018, with an initial speed in the LASCO CME catalog of greater than 1000 km/s. All CMEs were associated with M or X class flares, and corresponding interplanetary CMEs (ICMEs) were observed on the Earth. Both IPS observations of ISEE and white-light observations of LASCO were available during their propagation, and real-time simulation results for the arrival times were archived in the CME arrival-time scoreboard (Riley et al. 2018) of the Community Coordinated Modeling Center (CCMC). Our simulation could not forecast the arrival of some CMEs that occurred around the solar limb; therefore, these CMEs were removed from the evaluation of arrival-time error. It should also be noted that we removed some CME events despite the above criteria being satisfied for a variety of reasons; for example, CME-CME interaction during propagation. The 12 events that satisfy the criteria are listed in Table 1.

Table 1
CME characteristics investigated in this study and their observed and forecasted arrival times.

CME		CUCTus				LASCO			IPS			
Onset time	X-ray Class	Longitude	Latitude	Arrival time	Arrival time	Speed	abs(diff)	Arrival time	Speed	abs(diff)	Arrival time	Speed
2013/3/15	X1.2	-12	11	2013-03-17T05:28	2013/3/16 21:46	1879	7.70	2013/3/17 8:49	1366	3.35	2013/3/17 1:18	1666
2014/1/7	X1.2	11	15	2014-01-09T19:32	2014/1/9 1:27	1926	18.08	2014/1/9 2:13	1830	17.32	2014/1/9 5:24	1430
2014/4/2	M6.5	-53	14	2014-04-05T09:40	2014/4/5 14:34	1953	4.91	2014/4/5 22:47	1471	13.12	2014/4/5 14:34	1471
2014/4/18	M7.3	34	-20	2014-04-20T10:22	2014/4/20 14:18	1008	3.94	2014/4/20 11:02	1203	0.68	2014/4/20 11:02	1203
2014/9/10	X1.6	-2	14	2014-09-12T15:26	2014/9/12 3:40	1302	11.76	2014/9/12 3:57	1267	11.48	2014/9/12 3:40	1267
2015/6/18	M3.0	-50	15	2015-06-21T15:40	2015/6/21 10:43	1025	4.94	2015/6/21 8:04	1305	7.59	2015/6/21 5:18	1605
2015/6/21	M2.6	-16	12	2015-06-22T17:59	2015/6/22 16:57	1209	1.02	2015/6/22 18:14	1366	0.27	2015/6/22 15:44	1666
2015/6/22	M6.5	8	12	2015-06-24T12:57	2015/6/24 2:32	1953	10.40	2015/6/24 14:32	1209	1.59	2015/6/24 10:53	1609
2015/6/25	M7.9	42	9	2015-06-27T03:30	2015/6/27 8:17	1838	4.79	2015/6/27 13:26	1627	9.94	2015/6/27 6:42	1827
2017/7/14	M2.4	29	-6	2017-07-16T05:14	2017/7/16 3:38	1644	1.60	2017/7/16 10:09	1200	4.93	2017/7/16 4:16	1600
2017/9/4	M5.5	11	-10	2017-09-06T23:08	2017/9/6 13:08	1953	9.98	2017/9/6 14:54	1418	8.22	2017/9/6 18:57	1018
2017/9/6	X9.3	34	-9	2017-09-07T22:30	2017/9/7 21:47	1955	0.71	2017/9/8 0:49	1571	2.32	2017/9/7 20:44	1971

Results

The forecasted arrival times for each CME are summarized in Table 1. In this table, the onset day, X-ray class and location of the corresponding flare, and arrival time of the observed CME are listed in columns 1–5. The simulated arrival times and the arrival-time errors of the simulation runs using CMEs with different initial speeds (CACTus maximum speed, LASCO initial speed, and the speed that best fits the IPS observations) are listed between columns 6–14. The real-time forecast result from the WSA-ENLIL-Cone model archived in the CCMC CME Score Board is listed in columns 15 and 16. For the IPS based forecasting, we selected the simulation run that best estimates the IPS observations. Therefore, if the CME with the initial speed estimated from LASCO shows the best match to the IPS, IPS and LASCO based forecasting will exhibit the same arrival time.

Arrival-time error

Figure 3 shows a histogram of the absolute arrival-time errors. The average arrival-time error for CMEs with the initial speed derived from CACTus, LASCO, and the best fit to IPS is 6.7 h, 6.7 h, and 5.0 h, respectively. The corresponding arrival-time error for the WSA-Enlil-cone model archived in the CCMC CME score board is 12.7h. All simulation approaches resulted earlier average arrival-time prediction, i.e. the average of predicted arrival times is earlier than the average of actual arrival times.

Longitudinal and initial speed dependence of the arrival-time error

Figure 4a shows the relationship between the predicted arrival-time error and the initial speed of the CMEs, whereas Figure 4b shows the relationship between the predicted arrival-time error and the longitude of the CME location. No relationship is observed between the arrival-time error and either initial speed or longitude.

[1]<http://sidc.be/cactus/>

[2]https://cdaw.gsfc.nasa.gov/CME_list/

[3]<https://omniweb.gsfc.nasa.gov/>

[4]<https://kauai.ccmc.gsfc.nasa.gov/CMEscoreboard/>

Summary And Discussion

Loading [MathJax]/jax/output/CommonHTML/jax.js

Differences in the arrival-time error

IPS data improved the arrival time forecast of the MHD simulation compared to that derived from the MHD simulation without IPS data by 1.7 h (25%). In the majority of cases, IPS provided a better or equal arrival time; the IPS provided a worse arrival time in only two of 12 cases (Table 1). Moreover, the IPS-based MHD simulation significantly improved the arrival-time forecast in two CME events (2014-04-02 and 2015-06-25), which resulted in large arrival-time errors when forecast by the MHD simulation without IPS. From the perspective of space weather forecasting, a large arrival-time error can have serious consequences, which suggests that IPS data play a crucial role in the forecasting system.

The approach employed in this study provided better arrival-time forecasts than the real-time operated WSA-ENLIL-cone model, even without IPS data. This may be because our simulation used a spheromak instead of a cone as the CME model, resulting in a more realistic reconstruction of CME propagation. Moreover, the magnetic flux, radial width, and longitudinal width of the spheromak were assumed to be proportional to the X-ray flux of the corresponding flare (see Methods section). This assumption can cause the improvement of the arrival-time error.

Our simulation approach resulted in earlier arrival-time predictions, which is consistent with previous MHD simulations (Wold et al. 2018). If the magnetic field flux of the spheromak is too strong, acceleration and expansion of the CME can be overestimated, which may result in an earlier prediction. If the size of the CME is too small, the drag force from the background solar wind can be underestimated, which can also result in an earlier prediction. Furthermore, a radio scattering region may exist in front of the CME (Gothoskar and Rao, 1999), which could result in early prediction even when using IPS data.

Causes of the arrival-time error

The simulations that best fit the IPS data still exhibited arrival-time errors. In this study, we only optimized the initial speed of the CME; the other parameters were approximately assumed from GOES and LASCO observations. These assumptions should be optimized in future studies. Some CME parameters assumed in this study can be derived from LASCO white-light images by fitting the CME geometry using models such as the graduated cylindrical shell model (e.g., Thernisien et al. 2006). CMEs propagating in interplanetary space can be derived from the Heliospheric Imager onboard STEREO satellites (Mostl et al 2014; Howard 2015). White-light coronagraph data can also be estimated from our MHD simulations by calculating the Thomson scattering along the line of sight. Therefore, we may be able to optimize the CME parameters other than the initial speed by combining IPS observations, white-light observations, and MHD simulations.

The velocity, density, and temperature of background solar wind in our simulation were obtained from empirical models. These models have ambiguities and result in CME arrival-time errors because the interactions between background solar wind and CMEs can affect the propagation of CMEs (e.g., Chen 1996; Vršnak and Gopalswamy 2002). Background solar wind velocity can also be derived from IPS observations using the tomography technique (Kojima et al. 1998; Jackson et al 1998), and the derived velocity distribution can be adopted as the inner boundary of the global MHD simulation (Jackson et al. 2015). Future models should include IPS data for both CMEs and background solar winds.

Application to the space weather forecasting system

The approach employed in this study has been partially installed in the space weather forecasting system of the National Institute of Information and Communications Technology (NICT), which is the Japanese space weather forecasting center. During daily operation, CME arrival times should be forecasted as soon as possible after a CME is observed and the initial forecast should be given automatically or semi-automatically by human forecasters with a large error range. IPS observations can be made available approximately 1–2 days after the onset of CMEs exhibiting typical speeds. Therefore, our system can be used to limit the range of the initial forecast, which is similar to the data assimilation forecasts of typhoon trajectories. The combination of simulation and data assimilation techniques is expected to further improve the accuracy of CME arrival-time forecasts.

Abbreviations

CCMC
community coordinated modeling center
CACTus
computer aided CME tracking software
CME
coronal mass ejection
GOES
geostationary operational environmental satellite
IPS
interplanetary scintillation
LASCO
large angle and spectrometric coronagraph
MHD
magnetohydrodynamic
STEREO
solar terrestrial relations observatory
SOHO
solar and heliospheric observatory

Loading [MathJax]/jax/output/CommonHTML/jax.js

space-weather-forecast-usable system anchored by numerical operations and observations
SWIFT
solar wind imaging facility

Declarations

Ethics approval and consent to participate

Not applicable

Consent for publication

Not applicable

Availability of data and materials

The datasets supporting the conclusions of this article are available in the data repository of ISEE, Nagoya University http://stsw1.isee.nagoya-u.ac.jp/ips_data-e.html, Virtual Solar Observatory <https://sdac.virtualsolar.org/cgi/search>, and OMNIweb service <https://omniweb.gsfc.nasa.gov/>.

Competing interests

The authors declare that they have no competing interests.

Funding

This work was supported by the Ministry of Education, Culture, Sports, Science and Technology (MEXT), Japan Society for the Promotion of Science (JSPS), KAKENHI Grant Number 18H04442, 15H05813, and 15H05814.

Authors' contributions

KI led this study and drafted the manuscript. DS developed the MHD simulation codes. KI, MT, and KF operated and maintained the IPS radio observations. DS, MD, and YK operated and maintained the space weather forecasting system based on the MHD simulations. All authors read and approved the final manuscript.

Acknowledgements

This work was supported by MEXT/JSPS KAKENHI Grant Number 18H04442, 15H05813 and 15H05814. The IPS observations were provided by the solar wind program of the Institute for Space-Earth Environmental Research (ISEE). This study was conducted using the computational resources of the Center for Integrated Data Science, ISEE, Nagoya University, through a joint research program. We thank the LASCO coronagraph group for the white-light CME images.

References

1. Arge CN, Pizzo VJ (2000) Improvement in the prediction of solar wind conditions using near-real time solar magnetic field updates. *J Geophys Res* 105:10465–10480. doi:10.1029/1999JA000262
2. Arge CN, Luhmann JG, Odstrcil D, Schrijver CJ, Li Y (2004) Stream structure and coronal sources of the solar wind during the May 12th, 1997 CME. *J Atmos Solar Terr Phys* 66:1295–1309. doi:10.1016/j.jastp.2004.03.018
3. Brueckner GE, Howard RA, Koomen MJ, Korendyke CM, Michels DJ, Moses JD, Socker DG, Dere KP, Lamy PL, Llebaria A, Bout MV, Schwenn R, Simnett GM, Bedford DK, Eyles CJ (1995) The Large Angle Spectroscopic Coronagraph (LASCO). *Solar Phys* 162:357–402. doi:10.1007/BF00733434
4. Chen J (1996) Theory of prominence eruption and propagation: Interplanetary consequences. *J Geophys Res* 101:27499–27520. doi:10.1029/96JA02644
5. Gapper GR, Hewish A, Purvis A, Duffett-Smith PJ (1982) Observing interplanetary disturbances from the ground. *Nature* 296:633–636. doi:10.1038/296633a0
6. Glyantsev AV, Tyul'bashev SA, Chashei IV, Shishov VI (2015) Interplanetary-scintillation observations of coronal mass ejections near the maximum of the 24th solar-activity cycle. *Astronomy Rep* 59:40–45. doi:10.1134/S1063772915010047
7. Gopalswamy N, Lara A, Yashiro S, Kaiser ML, Howard RA (2001) Predicting the 1-AU arrival times of coronal mass ejections. *J Geophys Res* 106:29207–29218. doi:10.1029/2001JA000177
8. Gothoskar P, Rao AP (1999) On observing mass ejections in the interplanetary medium. *Solar Phys* 185:361–390. doi:10.1023/A:1005114622634

9. Hayashi K, Kojima M, Tokumaru M, Fujiki K (2003) MHD tomography using interplanetary scintillation measurement. *J Geophys Res (Space Physics)* 108:1102. doi:10.1029/2002JA009567
10. Hewish A, Scott PF, Wills D (1964) Interplanetary scintillation of small diameter radio sources. *Nature* 203:1214–1217. doi:10.1038/2031214a0
11. Howard TA (2015) Measuring an Eruptive Prominence at Large Distances from the Sun. II. Approaching 1 AU. *Astrophys J* 806:176. doi:10.1088/0004-637X/806/2/176
12. Iwai K, Shiota D, Tokumaru M, Fujiki K, Den M, Kubo Y (2019) Development of a coronal mass ejection arrival time forecasting system using interplanetary scintillation observations. *Earth Planets Space* 71:39. doi:10.1186/s40623-019-1019-5
13. Jackson BV, Hick PL, Kojima M, Yokobe A (1998) Heliospheric tomography using interplanetary scintillation observations 1. Combined Nagoya and Cambridge data. *J Geophys Res* 103:12049–12068. doi:10.1029/97JA02528
14. Jackson BV, Odstrcil D, Yu H-S, Hick PP, Buffington A, Mejia-Ambriz JC, Kim J, Hong S, Kim Y, Han J, Tokumaru M (2015) The UCSD kinematic IPS solar wind boundary and its use in the ENLIL 3-D MHD prediction model. *Space Weather* 13:104–115. doi:10.1002/2014SW001130
15. Johri A, Manoharan PK (2016) An Intense Flare-CME Event in 2015: Propagation and interaction effects between the Sun and Earth's orbit. *Solar Phys* 291:1433–1446. doi:10.1007/s11207-016-0900-7
16. Kageyama A, Sato T (2004) Yin-Yang grid: An overset grid in spherical geometry. *Geochem Geophys Geosystem* 5:Q09005. doi:10.1029/2004GC000734
17. Kojima M, Tokumaru M, Watanabe H, Yokobe A, Asai K, Jackson BV, Hick PL (1998) Heliospheric tomography using interplanetary scintillation observations 2. Latitude and heliocentric distance dependence of solar wind structure at 0.1-1 AU. *J Geophys Res* 103:1981–1990. doi:10.1029/97JA02162
18. Lee CO, Arge CN, Odstrcil D, Millward G, Pizzo V, Quinn JM, Henney CJ (2013) Ensemble Modeling of CME Propagation. *Solar Phys* 285:349–368. doi:10.1007/s11207-012-9980-1
19. Manoharan PK (2006) Evolution of Coronal Mass Ejections in the Inner Heliosphere: A Study Using White-Light and Scintillation Images. *Solar Phys* 235:345–368. doi:10.1007/s11207-006-0100-y
20. Millward G, Biesecker D, Pizzo V, de Koning CA (2013) An operational software tool for the analysis of coronagraph images: Determining CME parameters for input into the WSA-Enlil heliospheric model. *Space Weather* 11:57–68. doi:10.1002/swe.20024
21. Möstl C, Amla K, Hall JR, Liewer PC, De Jong EM, Colaninno RC, Veronig AM, Rollett T, Temmer M, Peinhart V, Davies JA, Lugaz N, Liu YD, Farrugia CJ, Luhmann JG, Vršnak B, Harrison RA, Galvin AB (2014) Connecting Speeds, Directions and Arrival Times of 22 Coronal Mass Ejections from the Sun to 1 AU. *Astrophys J* 787:119. doi:10.1088/0004-637X/787/2/119
22. Odstrcil D (2003) Modeling 3-D solar wind structure. *Advances Space Res* 32:497–506. doi:10.1016/S0273-1177(03)00332-6
23. Pomoell J, Poedts S (2018) EUHFORIA: European heliospheric forecasting information asset. *J Space Weather Space Climate* 8:A35. doi:10.1051/swsc/2018020
24. Riley P, Mays ML, Andries J, Amerstorfer T, Biesecker D, Delouille V, Dumbović M, Feng X, Henley E, Linker JA, Möstl C, Nuñez M, Pizzo V, Temmer M, Tobiska WK, Verbeke C, West MJ, Zhao X (2018) Forecasting the Arrival Time of Coronal Mass Ejections: Analysis of the CCMC CME Scoreboard. *Space Weather* 16:1245–1260. doi:10.1029/2018SW001962
25. Robbrecht E, Berghmans D (2004) Automated recognition of coronal mass ejections (CMEs) in near-real-time data. *Astronomy Astrophys* 425:1097–1106. doi:10.1051/0004-6361:20041302
26. Shiota D, Kataoka R, Miyoshi Y, Hara T, Tao C, Masunaga K, Futaana Y, Terada N (2014) Inner heliosphere MHD modeling system applicable to space weather forecasting for the other planets. *Space Weather* 12:187–204. doi:10.1002/2013SW000989
27. Shiota D, Kataoka R (2016) Magnetohydrodynamic simulation of interplanetary propagation of multiple coronal mass ejections with internal magnetic flux rope (SUSANOO-CME). *Space Weather* 14:56–75. doi:10.1002/2015SW001308
28. Temmer M, Preiss S, Veronig AM (2009) CME Projection Effects Studied with STEREO/COR and SOHO/LASCO. *Sol Phys* 256:183–199. doi:10.1007/s11207-009-9336-7
29. Themisien AFR, Howard RA, Vourlidas A (2006) Modeling of Flux Rope Coronal Mass Ejections. *Astrophys J* 652:763–773. doi:10.1086/508254
30. Tokumaru M, Kojima M, Fujiki K, Maruyama K, Maruyama Y, Ito H, Iju T (2011) A newly developed UHF radiotelescope for interplanetary scintillation observations: Solar Wind Imaging Facility. *Radio Science* 46(F02):RS0. doi:10.1029/2011RS004694
31. Tokumaru M, Kojima M, Fujiki K, Yamashita M (2006) Tracking heliospheric disturbances by interplanetary scintillation. *Nonlinear Processes Geophys* 13:329–338. doi:10.5194/npg-13-329-2006
32. Tokumaru M, Kojima M, Fujiki K, Yamashita M, Yokobe A (2003) Toroidal-shaped interplanetary disturbance associated with the halo coronal mass ejection event on 14 July 2000. *J Geophys Res (Space Physics)* 108:1220. doi:10.1029/2002JA009574
33. Vršnak B, Gopalswamy N (2002) Influence of the aerodynamic drag on the motion of interplanetary ejecta. *J Geophys Res (Space Physics)* 107:1019. doi:10.1029/2001JA000120
34. Wang Y-M, Sheeley NR (1990) Solar Wind Speed and Coronal Flux-Tube Expansion. *Astrophys J* 355:726. doi:10.1086/168805
35. Wold AM, Mays ML, Taktakishvili A, Jian LK, Odstrcil D, MacNeice P (2018) Verification of real-time WSA-ENLIL + Cone simulations of CME arrival-time at the CCMC from 2010 to 2016. *J Space Weather Space Climate* 8:A17. doi:10.1051/swsc/2018005
36. Yashiro S, Gopalswamy N, Michalek G, St. Cyr OC, Plunkett SP, Rich NB, Howard RA (2004) A catalog of white light coronal mass ejections observed by the SOHO spacecraft. *J Geophys Res (Space Physics)* 109:A07105. doi:10.1029/2003JA010282
37. Young AT (1971) Interpretation of Interplanetary Scintillations. *Astrophys J* 168:543. doi:10.1086/151108

Figures

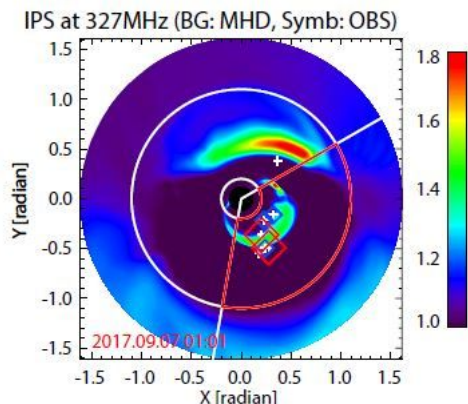


Figure 1

Example distribution of the simulated IPS data. IPS g-value estimated by the SUSANOO projected onto the sky-plane. White circles and red lines indicate elongation and position angle range of the radio source used for the forecasting, respectively. The symbols indicate the IPS g-value observed by SWIFT from 01:00 UT to 02:00 UT. Crosses indicate all observed radio sources and diamonds indicate radio sources with the following g-values: $2.0 < g$ (red), $1.5 < g < 2.0$ (green), and $1.2 < g < 1.5$ (blue).

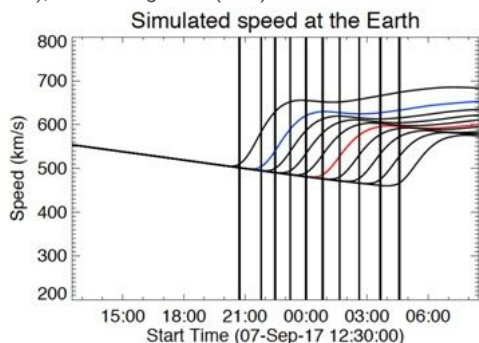


Figure 2

Example of the simulated solar wind speed at Earth. Solar wind speed at the Earth derived by simulation runs with CMEs with an initial speed derived from CACTus max speed (blue), the LASCO catalog (red), and eight CMEs with initial speeds that are faster or slower than the CME speed in the LASCO CME catalog with a 100-km/s interval (black). Vertical line indicates the arrival time of each CME at Earth.

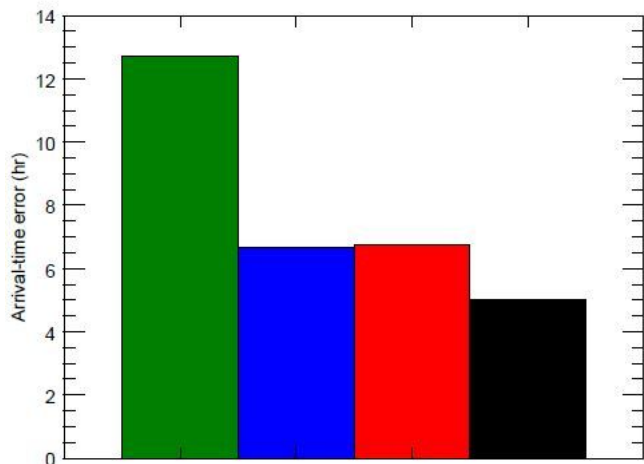


Figure 3

Histogram of the CME absolute arrival-time error at Earth. Average of the absolute arrival-time error at the Earth forecasted using different CME initial speeds. Colors indicate CMEs with initial speeds derived from CACTus (blue), the LASCO catalog (red), the best fit to IPS data (black), and real-time forecast result in archived the CCMC website (green).

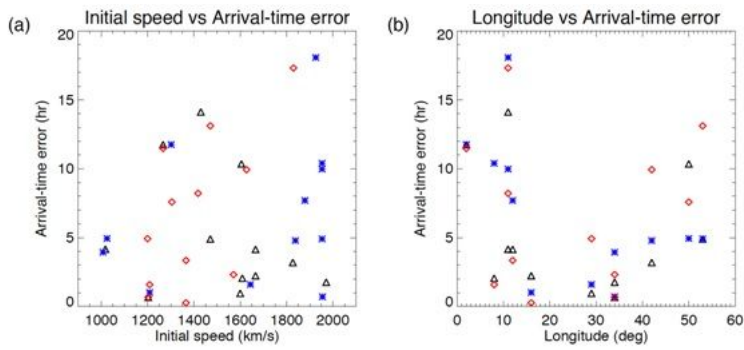


Figure 4

Initial speed and longitudinal dependence of the arrival-time error. (a) Relationship between predicted arrival-time error and initial speed of the CMEs. (b) Relationship between predicted arrival-time error and longitude of CME location. Colors indicate CMEs with initial speeds derived from CACTus (blue), the LASCO catalog (red), and the best fit to IPS data (black).

Supplementary Files

This is a list of supplementary files associated with this preprint. Click to download.

- [graphicalabstract.png](#)